Supporting Information

Core-shell polyoxometalate-based zeolite imidazole framework-derived multi-interfacial MoSe$_2$/CoSe$_2$@NC enabling multi-functional polysulfide anchoring and conversion in lithium-sulfur batteries

Lunan Zhang,[*a†] Tangsuo Li,[a†] Xuecheng Zhang,[a] Zhiyuan Ma,[a] Qiuping Zhou,[a] Yi Liu,[a] Xinyuan Jiang,[a] Hangyu Zhang,[a] Lubin Ni[*a] and Guowang Diao[*a]

[a] *School of Chemistry and Chemical Engineering, Yangzhou University, Yangzhou, 225002 (P.R. China)*

[*]Corresponding authors

E-mail address: zhangln@yzu.edu.cn (L.N. Zhang), lbni@yzu.edu.cn (L.B. Ni), gwdiao@yzu.edu.cn (G.W. Diao)

Postal address: Yangzhou University, Siwangting Road No. 180, Yangzhou, Jiangsu Province, 225002, P. R. China

Table of contents

Experimental Section

Chemicals and reagents

Cobalt nitrate (99.99%, AR), phosphomolybdic acid $H_3PMo_{12}O_{40} \cdot xH_2O$ and sublimed sulfur powder were obtained from Aladdin (China), Methanol (99.5%, AR) and 2-methylimidazole were purchased from Shanghai Chemical Reagents Company (Shanghai, China). Lithium sulfide (Li_2S) was purchased from Sigma Aldrich (USA).

Synthesis of PMo_{12}@ZIF-67 with different feeding ratios and pure ZIF-67

Briefly, a methanol (25 mL) solution of $Co(NO_3)_2 \cdot 6H_2O$ (0.72 g, 2.48 mmol) and an aqueous solution of PMo_{12} (10 mL DI H_2O, the masses of PMo_{12} were 25 mg, 50 mg and 100 mg, respectively) were mixed and stirred vigorously at room temperature for 30 minutes. Then 2-methylimidazole (1.63 g, 19.84 mmol) in 25 mL methanol was quickly added to the above solution, stirring for further 2.5 h. Finally, the obtained precipitates were centrifugally collected, and washed several times with methanol and deionized water. The solids were dried at 75 °C for 10 h to obtain the desired products. The obtained PMo_{12}@ZIF-67 with three different feeding ratios are noted as PMo_{12}@ZIF-67 (25 mg), PMo_{12}@ZIF-67 (50 mg) and PMo_{12}@ZIF-67 (100 mg). The procedure for the synthesis of pure ZIF-67 follows the same procedure in the absence of PMo_{12}.

Synthesis of NC

ZIF-67 was transferred to a porcelain boat in a tube furnace and heated at 350 °C for 2 h with a ramping rate of 2 °C min^{-1}. After that, the temperature was raised to 600 °C with the rate of 5 °C min^{-1} and maintained for 2 h. The entire heating process takes place in an atmosphere of Ar. After cooling down to room temperature, Co@NC was

collected. The Co@NC was etched with 2M HCl and further dried at 60 °C for 10 h to obtain the desired product of NC.

Synthesis of Mo-doped CoSe₂@NC

The synthesis of Mo-doped $CoSe_2$@NC is similar to that of the $MoSe_2$/$CoSe_2$@NC described in the manuscript, except that the precursor used was changed from PMo_{12}@ZIF-67 to PMo_{12}@ZIF-67 (25mg).

Materials Characterization

The structure of the sample was investigated by XRD (WAXD, D8 Advance, Bruker, Cu Kα, λ = 1.54 Å). TGA (Netzsch TG209 F3) measurements were collected from room temperature to 800 °C with a hating rate of 10 °C min⁻¹ under N_2/air flow. An XPS (Thermo Escalab 250 system) was used to determine the elemental composition of nanoparticles with Al Kα radiation (hv = 1486.6 eV) and the chamber pressure was kept below 2×10^{-9} Torr. SEM (Zeiss Supra-55 VP) was used to characterize the external morphology. TEM (Philips TECNAI-12) was used to characterize the microscopic structure of the samples. HRTEM and HAADF-STEM were measured under 200 kV by an FEI Themis Z (USA). BET surface areas of the sample were measured by the equipment of JW-BK 200 static nitrogen adsorption (Beijing Jingwei Gaobo Science and Technology Co. Ltd. China). UV-vis absorption spectra (UV/vis, Shimadzu UVmini-1280 spectrophotometer) were used to detect the concentration and elemental chemical states of the LiPSs.

LiPSs adsorption test

As a representative LiPSs, Li_2S_4/DME solution (0.04 M) was prepared by adding

384 mg of sulfur (12 mmol) and 184 mg of Li$_2$S (4.0 mmol) into 100 mL of DME solution under vigorous stirring according to previous reports. Before the adsorption experiment, 9 mL DME was added to the 1 mL prepared 0.04 M Li$_2$S$_4$/DME solution to dilute it 10-fold. Poured 50 mg of MoSe$_2$/CoSe$_2$@NC, CoSe$_2$@NC and NC into 10 mL of diluted Li$_2$S$_4$/DME solution separately, and stirred vigorously for 1 h. Then the solution was left to stand for 30 min and all supernatants after treatment with various sulfur hosts were analyzed by UV–vis spectroscopy. All operations were conducted in an argon-filled glove box.

Oxidation of Lithium Sulfide (Li$_2$S) Test

Firstly, Li$_2$S (20 mg) was added into DME (6 mL) solvent with stirring in a 20 mL penicillin bottle. Then 40 mg of various host materials (MoSe$_2$/CoSe$_2$@NC, CoSe$_2$@NC and NC) were also added to the reaction system separately with continuous stirring for 10 h. The solution was then left to stand for 30 min and all supernatants after treatment with various sulfur hosts were analyzed by UV-vis spectroscopy. All operations were conducted in an argon-filled glove box.

Li$_2$S$_6$ electrolyte based Symmetric Battery Assembly and Measurements

The electrodes of Li$_2$S$_6$ symmetric battery were composed of electrode materials (MoSe$_2$/CoSe$_2$@NC, CoSe$_2$@NC and NC), Super P, and polyvinylidene fluoride (PVDF) binder with the mass ratio of 7:2:1. The areal loading was all controlled around 1.5 mg cm^{-2}. The Li$_2$S$_6$ electrolyte (0.5 M) was prepared by adding sulfur (8 g) and Li$_2$S (2.3 g) in 100 mL of Li-S battery electrolyte (0.5 M lithium trifluoromethanesulfonate (LiCF$_3$SO$_3$) and 0.5 M LiNO$_3$ dissolved in 1,3-dioxolane (DOL) and

dimethoxymethane (DME) (volume ratio = 1: 1)) followed by vigorous mixing at room temperature for two weeks. Two identical electrodes ($MoSe_2/CoSe_2$@NC, $CoSe_2$@NC and NC), a Celgard 2500 separator and 40.0 μL Li_2S_6 electrolyte (0.5 M) were assembled into a standard CR2032 coin cell. The CV of symmetric cell was performed voltage window from -1.0 to 1.0 V at a scan rate of 10 mV s^{-1}.

In Situ UV-Vis Measurement

The cathode slurry was composed of the S@$MoSe_2/CoSe_2$@NC or S@$CoSe_2$@NC, Super P, and PVDF binder with a mass ratio of 7:2:1. Then, the nickel foam was selected as the collector (0.8 × 0.8 cm^2). The areal sulfur loading was around 5.0 mg cm^{-2}. The in-situ UV-Vis cells were assembled using the S@$MoSe_2/CoSe_2$@NC or S@$CoSe_2$@NC electrode as the cathode and lithium metal as the anode, using a custom made in situ cuvette. The in-situ cuvette battery was assembled in an argon-filled glove box and further sealed in 3 mL of Li-S battery electrolyte (0.5 M $LiCF_3SO_3$ and 0.5 M $LiNO_3$ dissolved in the mixture of 1,3-DOL and DME with volume ratio of 1: 1). In situ cuvette cell discharges at 0.02 C constant current in the potential range of 1.8-2.8 V. UV-vis spectra were recorded every 15 minutes from the beginning to the end of discharge in situ cuvette batteries.

Li-S Battery Assembly and Electrochemical Measurements

The active substances (S@$MoSe_2/CoSe_2$@NC, S@$CoSe_2$@NC and S@NC) were mixed with super P li (TIMCAL) and PVDF (HSV900) with a weight ratio of 7:2:1 in N-methyl pyrrolidone (NMP) to form a homogeneous slurry. After that, the obtained slurry was directly coated on carbon paper (GDL 28 AA, SGL) current collectors with

a diameter of 16.0 mm, which was further dried at 60 °C for 12 h. The low sulfur loading on each carbon paper is about ≈1.5 mg cm^{-2}. For comparison, a high area sulfur loading of ≈3.6 mg cm^{-2}. The 2032-type coin cells were assembled using the prepared electrode (S@MoSe$_2$/CoSe$_2$@NC, S@CoSe$_2$@NC and S@NC) as the cathode, Celgard 2500 microporous polypropylene (PP) as a separator and lithium foil as the anode (diameter: 16 mm; thickness: 0.6 mm) in an Ar-filled glove box. The Li-S battery electrolyte was prepared by 0.5 M LiCF$_3$SO$_3$ and 0.5 M LiNO$_3$ dissolved in DOL and DME (volume ratio = 1: 1). In addition, the amount of the electrolyte was strictly controlled for performance evaluation, and the cell contained an electrolyte to sulfur (E/S) ratio of ≈ 12 μL mg^{-1}. The galvanostatic charge/discharge tests were conducted on Neware Battery Measurement System CT 4008W (Neware, China) from 2.8 to 1.7 V at room temperature. The GITT tests of the second cycle were recorded, the closed-circuit voltage (CCV) was measured with a current pulse of 0.1 C for 5 min, and then the quasi-open circuit voltage (QOCV) was obtained by resting the battery for 20 min. For PITT measurements, the 2032-type coin cells were performed on the PITT module of the Gamry Electrochemical Workstation. The voltage range is 2.4-1.7 V, the voltage interval is -50 mV, and the cutoff condition is that the current response is less than 0.05 mA or the run time is greater than 15 min. Then the battery was left for 15 minutes to reach equilibrium. The charging procedure is similar to the discharging PITT, except that the voltage interval is 50 mV. Electrochemical impedance spectra (EIS) and cyclic voltammetry (CV) measurements were measured on a Chenhua CHI-660E electrochemical workstation. CV curves was performed from 2.8 V to 1.7 V (vs Li$^+$/Li)

at a scanning rate of 0.1 mV s^{-1}, and the frequency of EIS was performed form 100 kHz to 0.01 Hz at open-circuit potential.

Theoretical Section

Computational Methods

All the calculations results based on the DFT. The Geometry Optimizatio of the system used CASTEP module. And the plane wave code CASTEP with the generalized gradient approximation by Perdew-Burke-Ernzerhof. After the energy convergence testament, $3 \times 3 \times 1$ and $4 \times 4 \times 1$ Monkhorst-Pack meshes were used for the sampling of the Brillouin zone with a kinetic energy cut-off energy of 408.19 and 408.19 eV. The threshold for self-consistent-field (SCF) density convergence is 1.0×10^{-6} eV per atom. One Li_2S_4 molecule was adsorbed on only one side of the exposed surfaces, with the dipole moment corrected accordingly along the (100) and (100) directions. The binding energy (E_b) of the Li_2S_4 on $MoSe_2$ or $CoSe_2$ monolayer was calculated as follows: $E_{b1} = E(MoSe_2/Li_2S_4) - E(Li_2S_4) - E(MoSe_2)$, $E_{b2} = E(CoSe_2/Li_2S_4) - E(Li_2S_4) - E(CoSe_2)$, where $E(MoSe_2)$, $E(CoSe_2)$, $E(Li_2S_4)$, $E(MoSe_2/Li_2S_4)$, and $E(CoSe_2/Li_2S_4)$ represent the total energies of the $MoSe_2$ and $CoSe_2$ substrate, the Li_2S_4 molecule, and the adsorption pair of the $MoSe_2$ substrate and Li_2S_4, $CoSe_2$ and Li_2S_4, respectively.
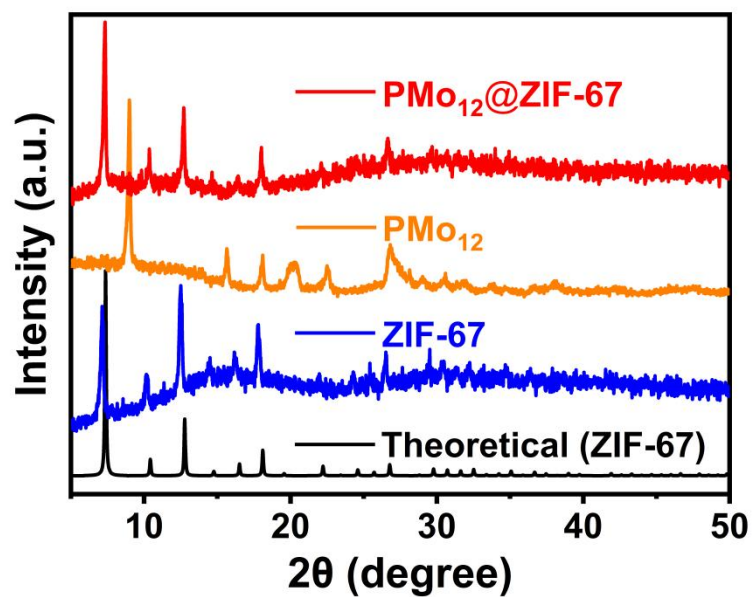
Supporting Figures

Fig. S1. The PXRD patterns of ZIF-67, PMo_{12} and PMo_{12}@ZIF-67.

As shown in **Fig. S1**, the PXRD pattern of obtained ZIF-67 matches well with the theoretical value, indicating the successful synthesis of ZIF-67. In addition, the characteristic peaks belonging to ZIF-67 and PMo_{12} can be clearly observed in the PXRD pattern of PMo_{12}@ZIF-67, which reflects that PMo_{12} has been encapsulated in the channel of ZIF-67 without changing its original crystal structure.
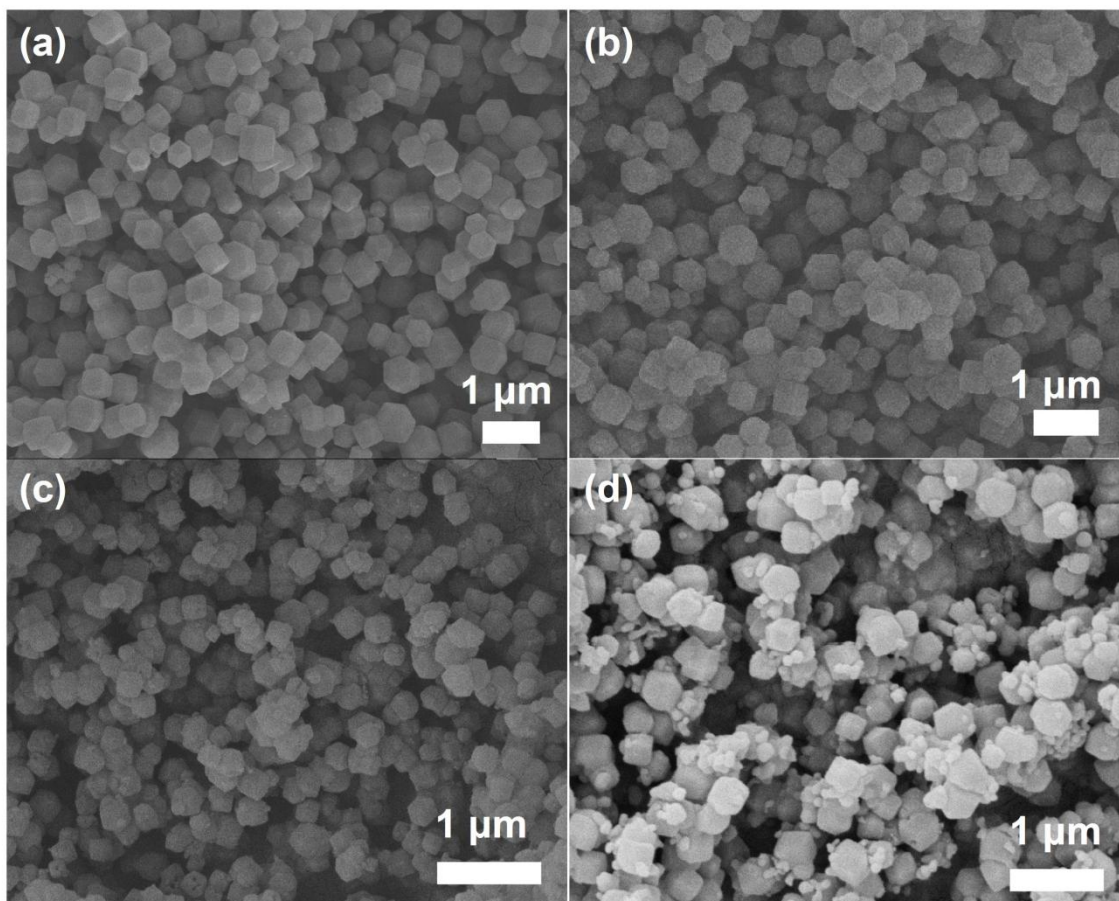
Fig. S2. (a) SEM image of ZIF-67; (b) SEM image of PMo_{12}@ZIF-67 (25mg); (c) SEM image of PMo_{12}@ZIF-67 (50mg); (d) SEM image of PMo_{12}@ZIF-67 (100mg).

The SEM image of pure ZIF-67 is shown in **Fig. S2a**, the regular polyhedral morphology can be found. As displayed in **Fig. S2b-S2c**, it is unambiguous to discover that the regular polyhedral shape of ZIF-67 can be well maintained after the encapsulation of 25 mg or 50 mg PMo_{12}. However, as shown in **Fig. S2d**, a large number of PMo_{12} nanoparticles were found on the surfaces of ZIF-67 after the addition of 100 mg PMo_{12}, indicating that the cavity of ZIF-67 was filled with PMo_{12}.
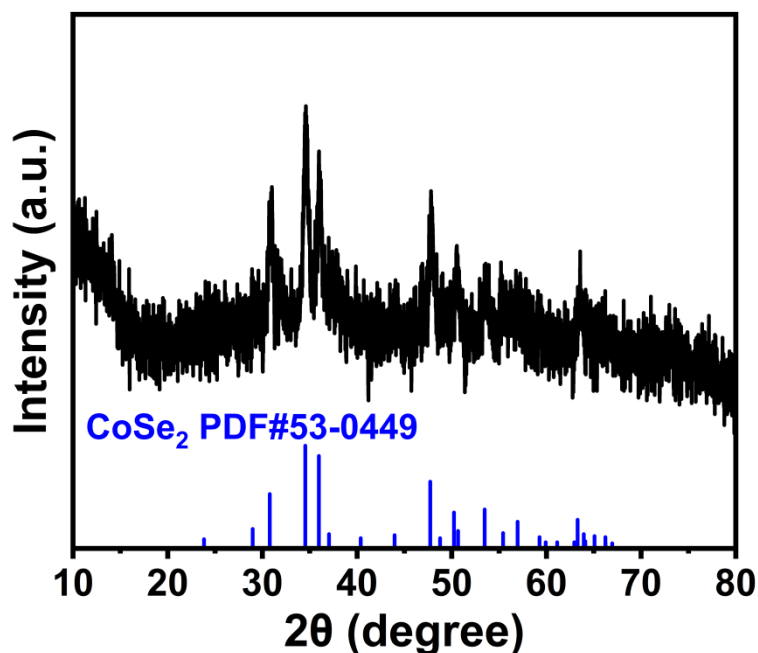
Fig. S3. The PXRD pattern of Mo-doped $CoSe_2$@NC.

The PXRD spectra of Mo-doped $CoSe_2$ was analyzed. There are several strong diffraction peaks appeared at 30.8, 34.5, 35.9 and 47.7 should be attributed to (101), (111), (120) and (211) planes of $CoSe_2$ (PDF#53-0449), respectively. Meanwhile, there exists several weak peaks located at 50.2, 53.5 and 63.3 degree are ascribed to (002), (031) and (122) lattice planes of $CoSe_2$. However, no diffraction peaks corresponding to $MoSe_2$ were observed, which may be due to the low Mo content in the precursor of PMo_{12}@ZIF-67 (25mg), which prevented the formation of crystalline $MoSe_2$ phase during selenization.

Considering the above results presented in **Fig. S2-S3**, we choose PMo_{12}@ZIF-67 (50mg) as the precursor for subsequent selenization in this work. Additionally, all of the PMo_{12}@ZIF-67 (50mg) mentioned in this article are simplified as PMo_{12}@ZIF-67.
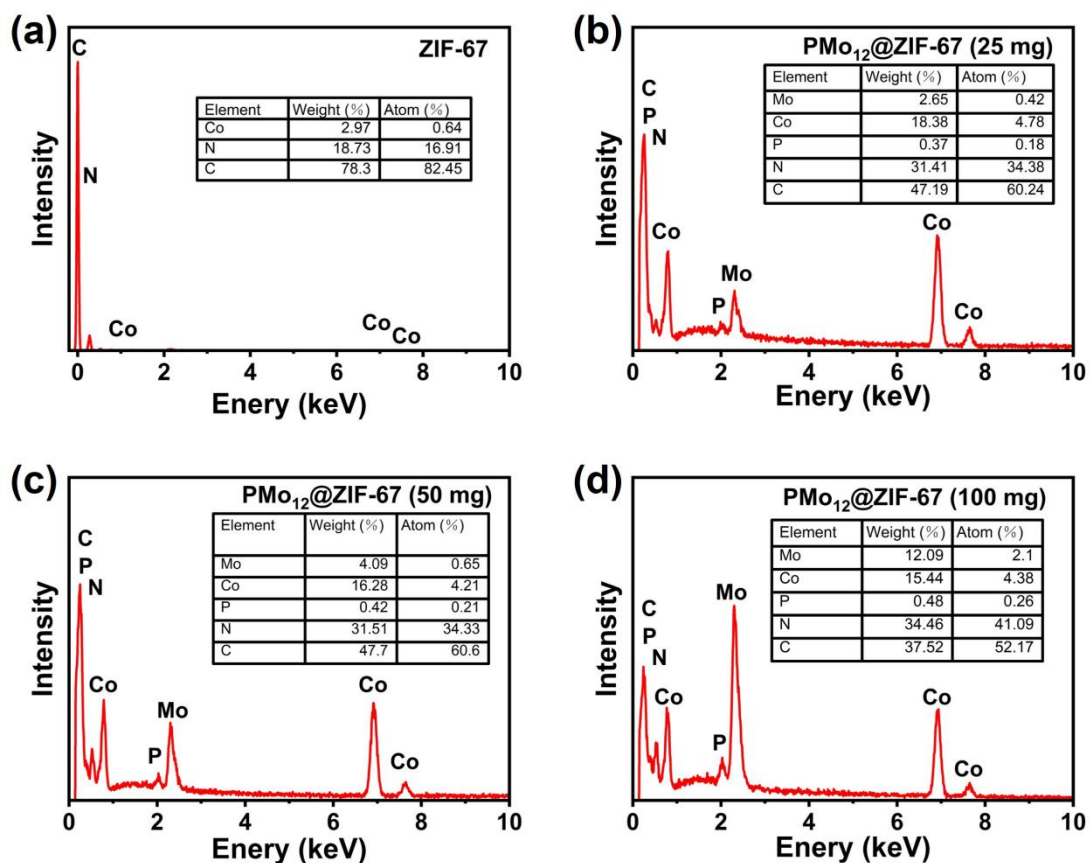
Fig. S4. EDAX spectra of (a) ZIF-67, (b)-(d) series of PMo$_{12}$@ZIF-67 with different PMo$_{12}$ mass loading.
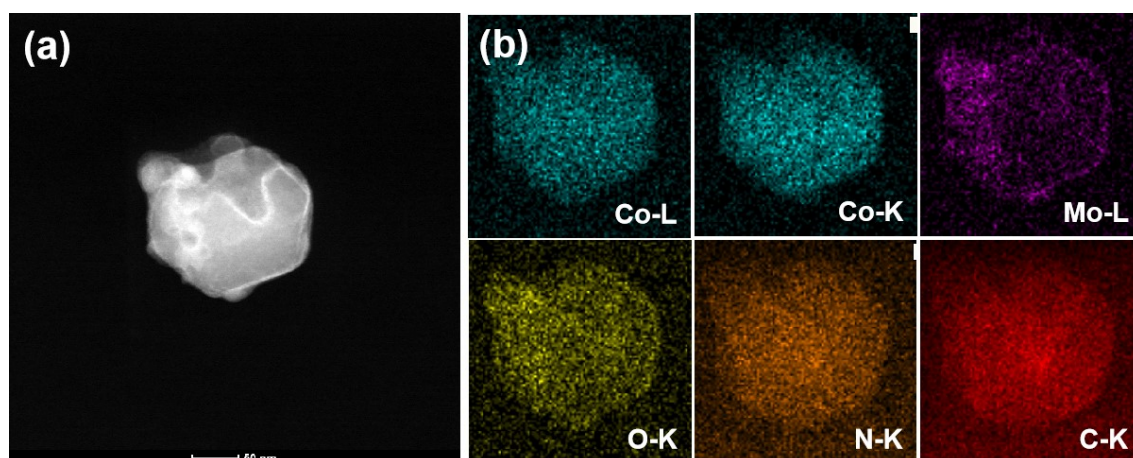

Fig. S5. (a-b) Dark field STEM images of the PMo$_{12}$@ZIF-67 and EDX elemental mapping on Co, Mo, O, N and C.

The Energy-dispersive X-ray spectroscopy (EDX) elemental mapping give an

effective demonstration of the $PMo_{12}@ZIF-67$, confirming the $PMo_{12}@ZIF-67$ contains Co, Mo, O, N and C elements. The uniform distribution of elements further proves that $PMo_{12}@ZIF-67$ has been prepared.
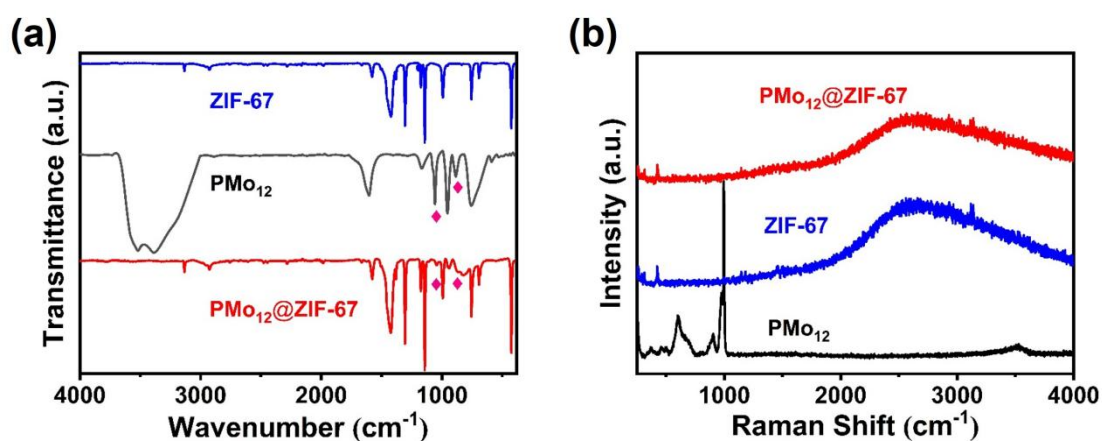
Fig. S6. (a) IR spectra and (b) Raman spectra of ZIF-67, PMo_{12} and $PMo_{12}@ZIF-67$.

In the infrared (IR) spectrum of $PMo_{12}@ZIF-67$, two new peaks indexing to PMo_{12} can be observed, which is absent for ZIF-67, implying that PMo_{12} is indeed encapsulated in ZIF-67 cage. Furthermore, the Raman spectra are also tested.
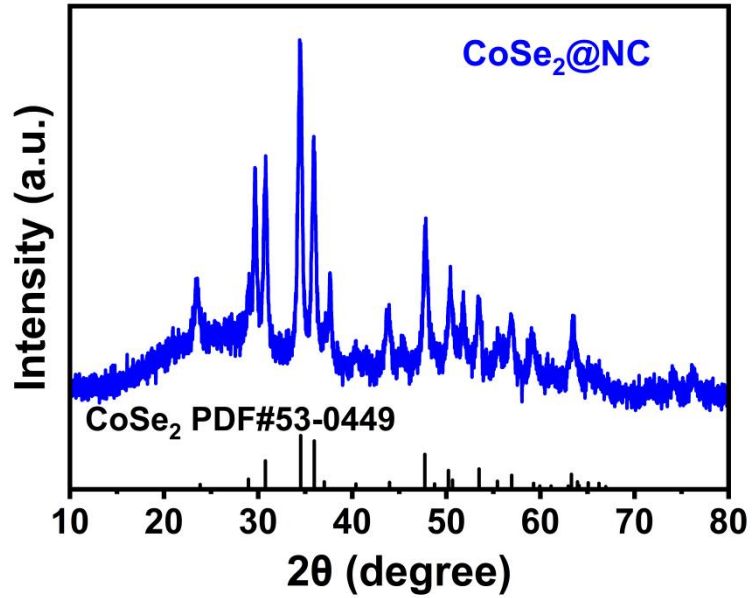
Fig. S7. PXRD pattern of $CoSe_2$@NC.

The PXRD of $CoSe_2$@NC was analyzed. There are several strong diffraction peaks at $2\theta \approx 30.8$, 34.5, 35.9, 47.7 and 50.6 degree, which are attributed to (101), (111), (120), (211) and (130) lattice planes of $CoSe_2$ (PDF#53-0449). Meanwhile, there exists several weak peaks located at 50.2, 53.5 and 63.3 degree are ascribed to the (002), (031) and (122) lattice planes of $CoSe_2$.
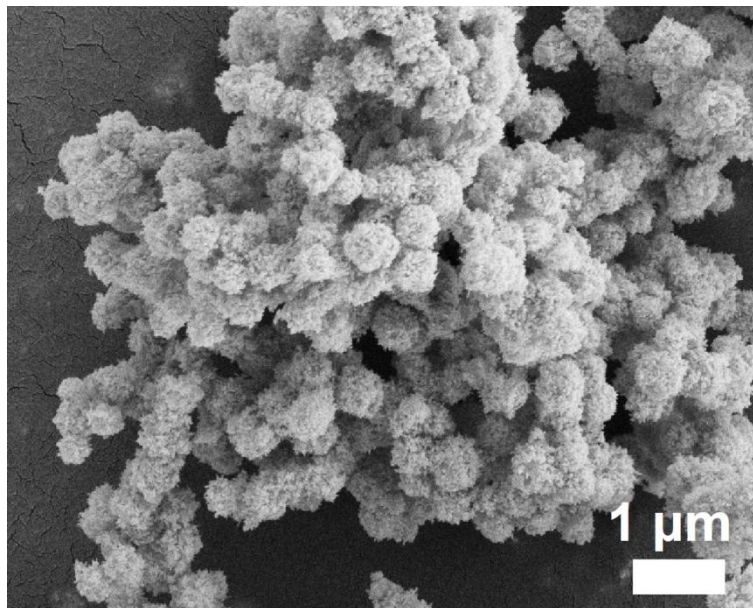

Fig. S8. SEM image of the $CoSe_2$@NC.

Fig. S8 shows the SEM image of the CoSe$_2$@NC, we can find that the morphology of CoSe$_2$@NC is similar to that of MoSe$_2$/CoSe$_2$@NC, and basically inherits the polyhedral morphology of PMo$_{12}$@ZIF-67.

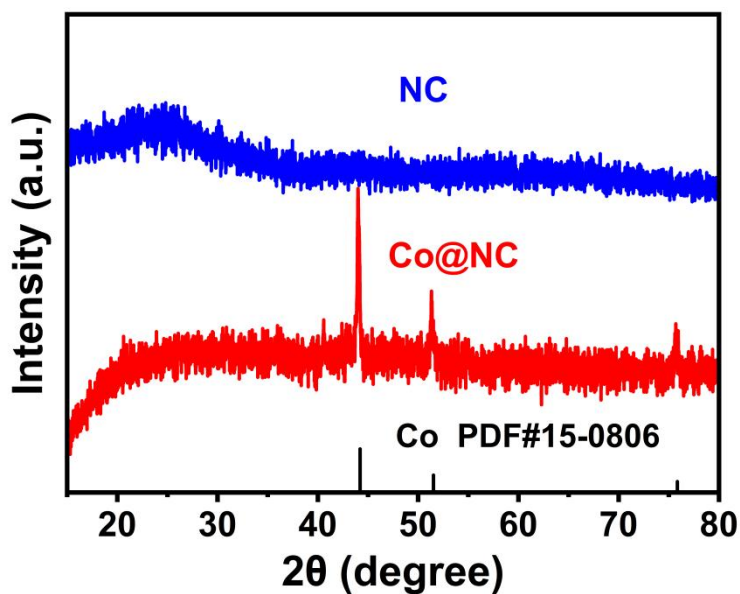**Fig. S9.** PXRD patterns of the Co@NC and NC.

In the PXRD pattern of Co@NC, there are three strong diffraction peaks appeared 44.2, 51.5 and 75.8, which should be attributed to (111), (200), and (220) lattice planes of Co (PDF#15-0806). After acid etching, these characteristic peaks both disappeared, implying that all of the Co nanoparticles are removed and the NC skeleton is obtained.
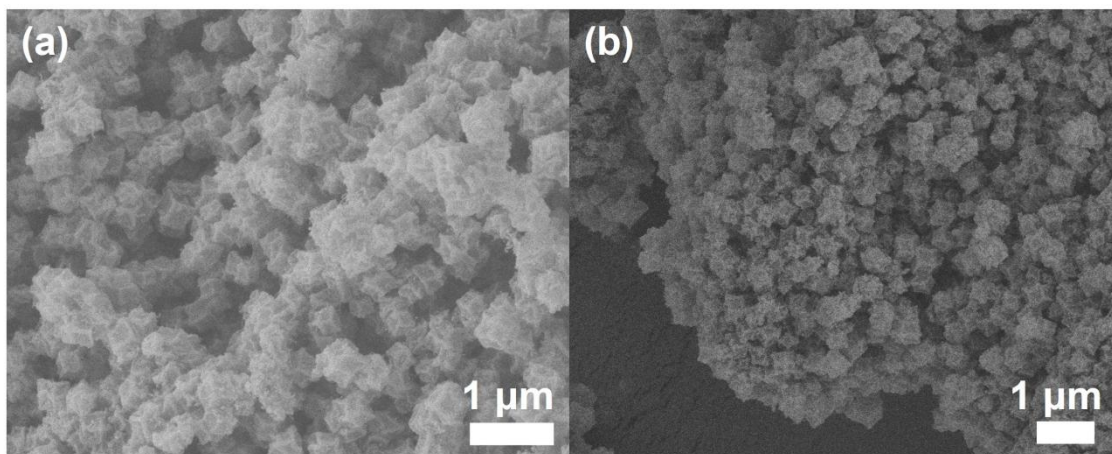
Fig. S10. (a) SEM image of the Co@NC; (b) SEM image of the NC.

As displayed in **Fig. S10**, Co@NC and NC show similar polyhedral morphology with crumpled surfaces.
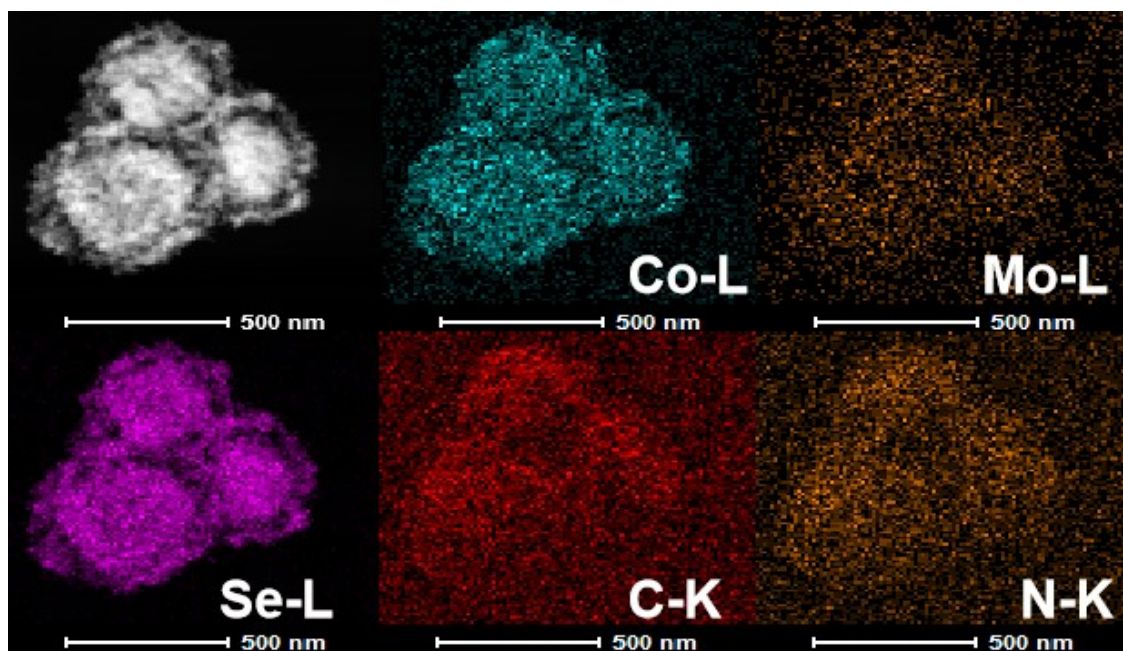

Fig. S11. Dark field STEM images of MoSe$_2$/CoSe$_2$@NC and the corresponding EDX elemental mapping of Co, Mo, Se, C and N.
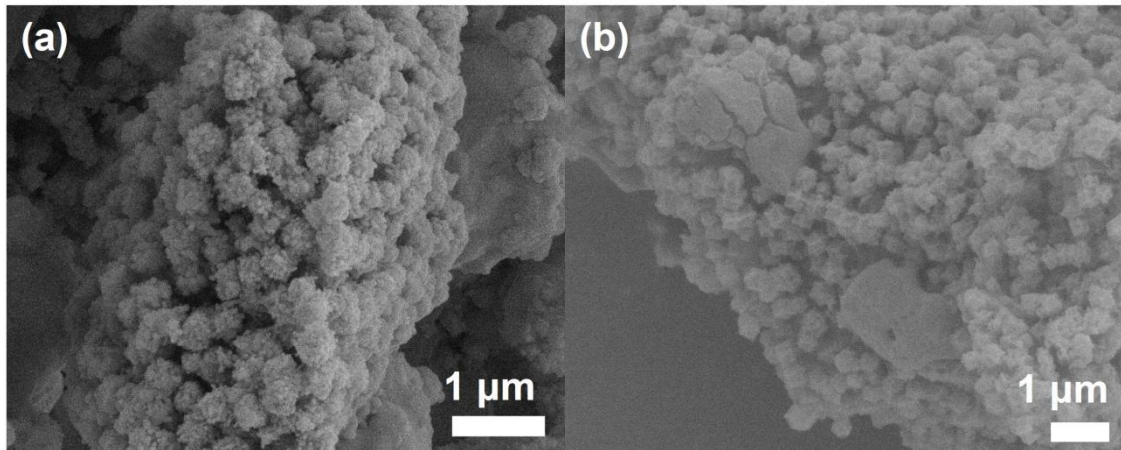
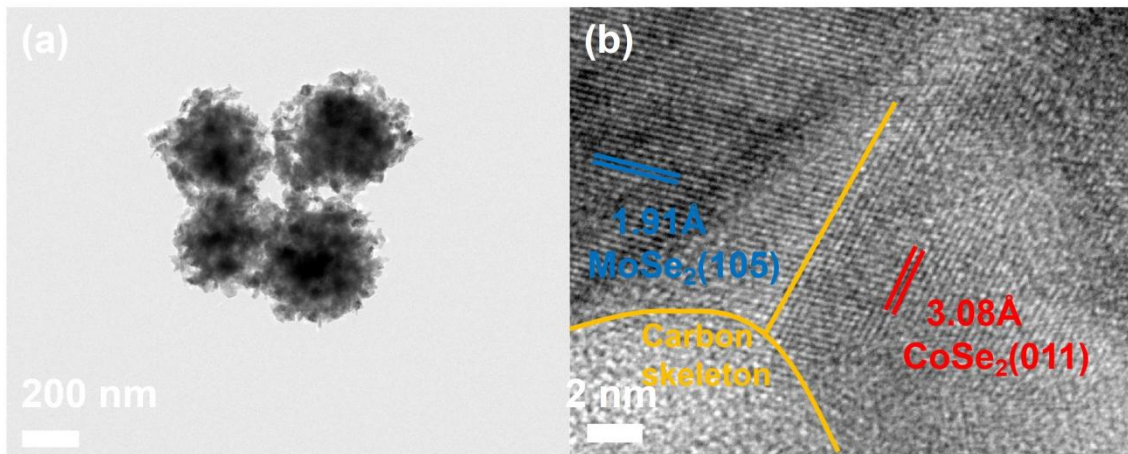**Fig. S12.** (a) SEM image of the S@CoSe$_2$@NC; (b) SEM image of the S@NC.

Fig. S13. (a) TEM and (b) HRTEM image of the S@MoSe$_2$/CoSe$_2$@NC.

Fig. S13 shows TEM image of the S@MoSe$_2$/CoSe$_2$@NC. Comparing with the MoSe$_2$/CoSe$_2$@NC, the core-shell structure of S@MoSe$_2$/CoSe$_2$@NC can still be clearly observed in several polyhedrons. The HRTEM image represents the lattice fringes with interplanar distances of 3.08 Å is associated with the (011) facets of CoSe$_2$, and the others with 1.91 Å correspond to the (105) crystallographic planes of MoSe$_2$.
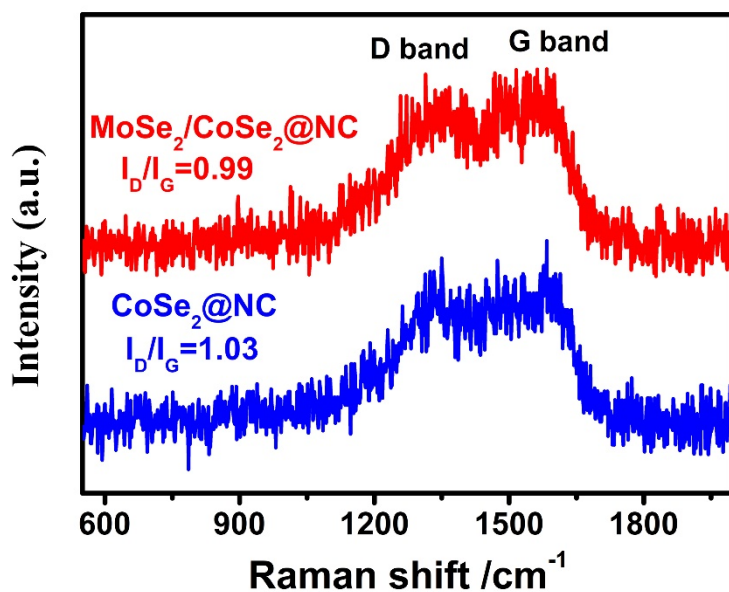
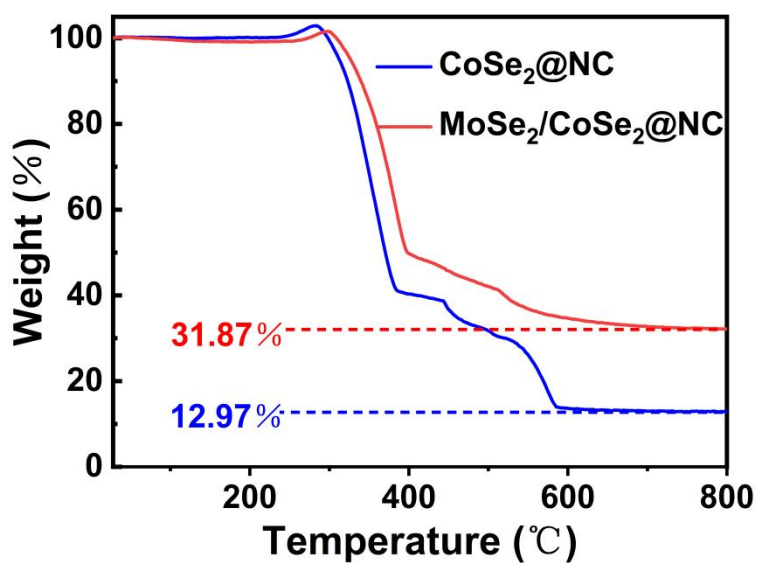**Fig. S14.** Raman spectra of $MoSe_2/CoSe_2@NC$ and $CoSe_2@NC$.

Fig. S15. TGA curves of $CoSe_2@NC$ and $MoSe_2/CoSe_2@NC$ in air.

The TGA curves reflect the decomposition of N-doped carbon species, and the oxidation of $CoSe_2$ and $MoSe_2$. It can be thermally decomposed at about 300 °C, indicating that $CoSe_2@NC$ and $MoSe_2/CoSe_2@NC$ have good thermal stability at the battery test temperature. The final residual amounts of Co_3O_4 and MoO_3 content at 700 °C for $CoSe_2@NC$ and $MoSe_2/CoSe_2@NC$ are 12.97 wt % and 31.87 wt%, respectively, which reflect that there are more host materials in $MoSe_2/CoSe_2@NC$ than
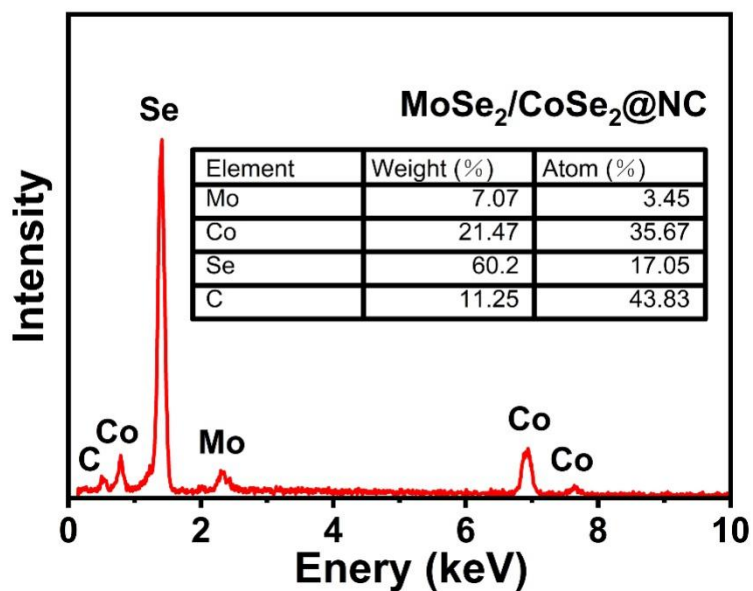
in CoSe$_2$@NC.

Fig. S16. EDX spectra of MoSe$_2$/CoSe$_2$@NC.

As can be seen from the results listed in the above table, the mass content of carbon

in MoSe$_2$/CoSe$_2$@NC is approximately 11.25%, while the element of N is not detected

due to the low content and the limited accuracy of the instrument. However, the real

presence of N has been confirmed in **Fig. 1l** of the manuscript. The atomic ratio of Co

and Mo is 4.94, which is close to 5. Therefore, we conclude that the molar ratio of

CoSe$_2$ phase to MoSe$_2$ phase in MoSe$_2$/CoSe$_2$@NC composite is approximately 5:1.
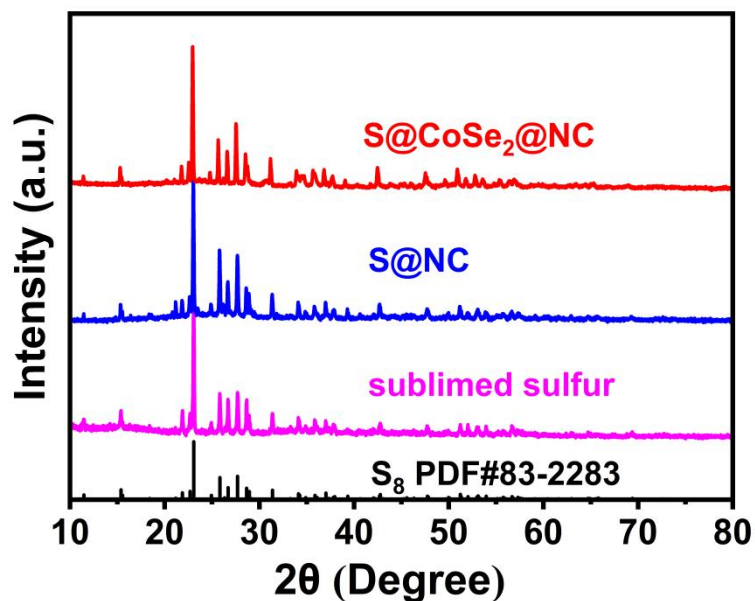
Fig. S17. The PXRD patterns S@CoSe$_2$@NC, S@NC composites and sublimed sulfur.

The strong diffraction peaks of sublimed sulfur are discovered in the PXRD pattern of S@NC and S@CoSe$_2$@NC, showing the successful loading of sulfur.
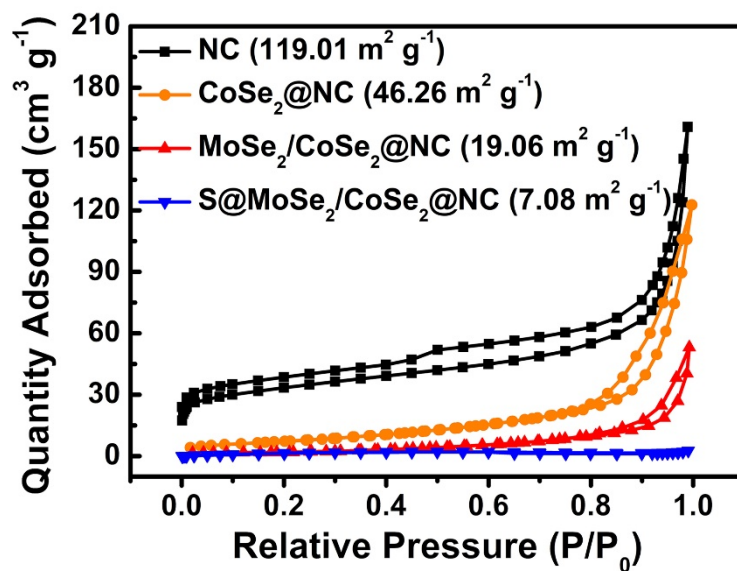

Fig. S18. N$_2$ adsorption - desorption isotherms for NC, CoSe$_2$@NC, MoSe$_2$/CoSe$_2$@NC and S@MoSe$_2$/CoSe$_2$@NC.
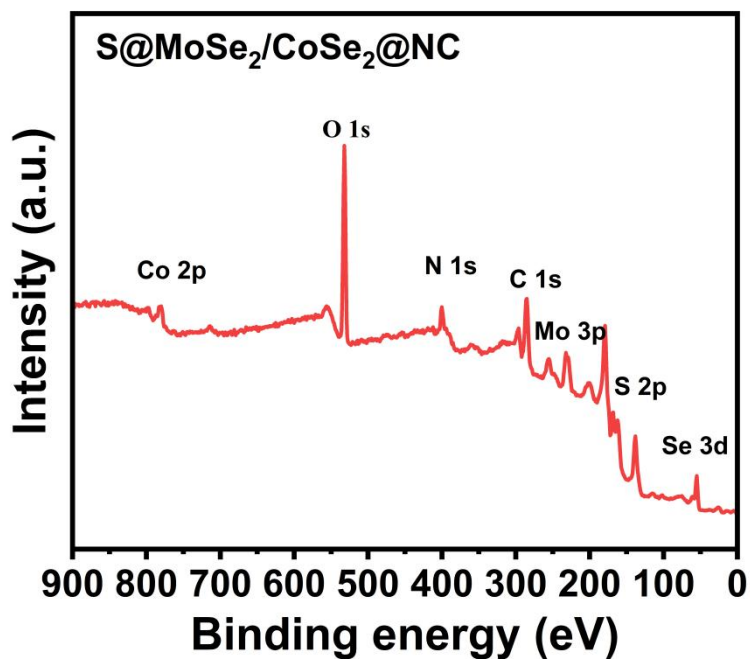
Fig. S19. XPS survey spectrum of the as-prepared S@MoSe$_2$/CoSe$_2$@NC composite.
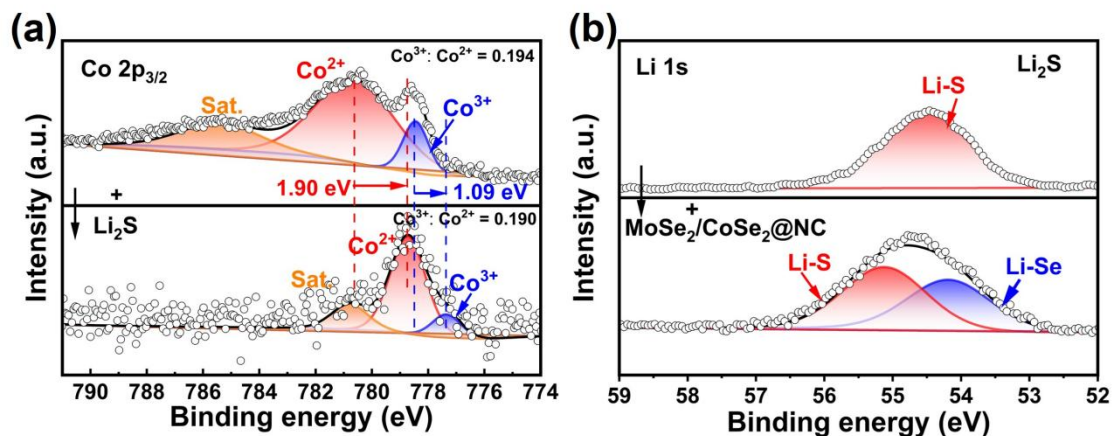
Fig. S20. (a) Co 2p$_{3/2}$ XPS spectra of MoSe$_2$/CoSe$_2$@NC and MoSe$_2$/CoSe$_2$@NC+Li$_2$S; (b) Li 1s XPS spectra of pristine Li$_2$S and MoSe$_2$/CoSe$_2$@NC+Li$_2$S.
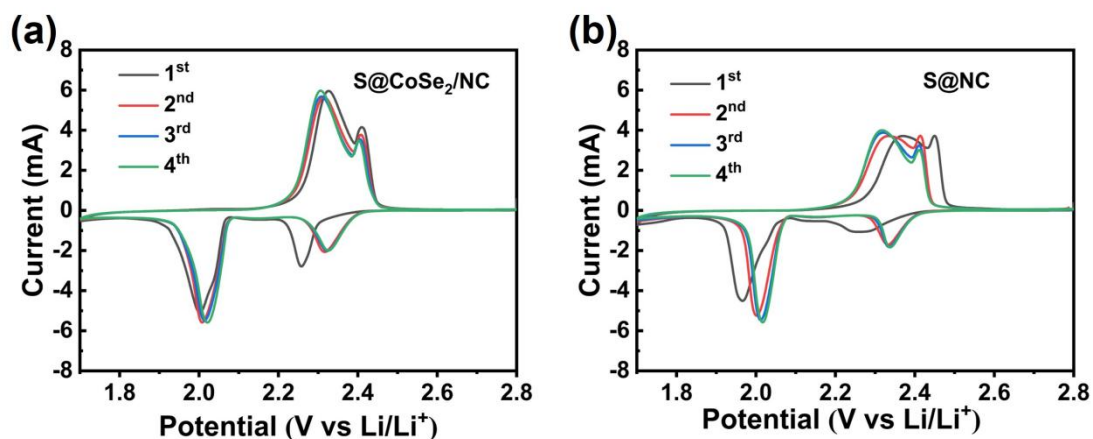
Fig. S21. (a) The CVs of S@CoSe$_2$@NC cathode material for the first four cycles; (b) The CVs of S@NC cathode material for the first four cycles.

The cyclic voltammograms (CVs) of the first four cycles of Li-S cells with S@CoSe$_2$@NC and S@NC composites at a scanning rate of 0.1 mV s^{-1}. Two peaks of reduction were observed in the reduction of S@CoSe$_2$@NC and S@NC, and two peaks of oxidation were also observed in the oxidation process, which was the same as for S@MoSe$_2$/CoSe$_2$@NC.

Fig. S22. The CVs of CoSe$_2$@NC symmetrical cells with Li$_2$S$_6$ electrolyte for the

first three cycles.
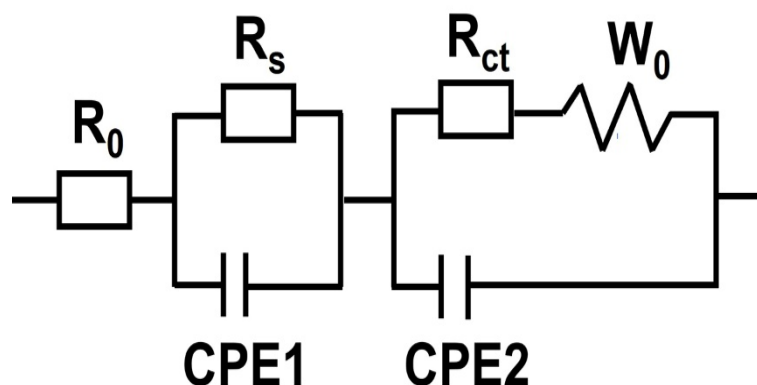
Fig. S23. The equivalent circuit of EIS.

R_o: The intercept at real axis Z' represents the Ohmic resistance R_o, corresponding to
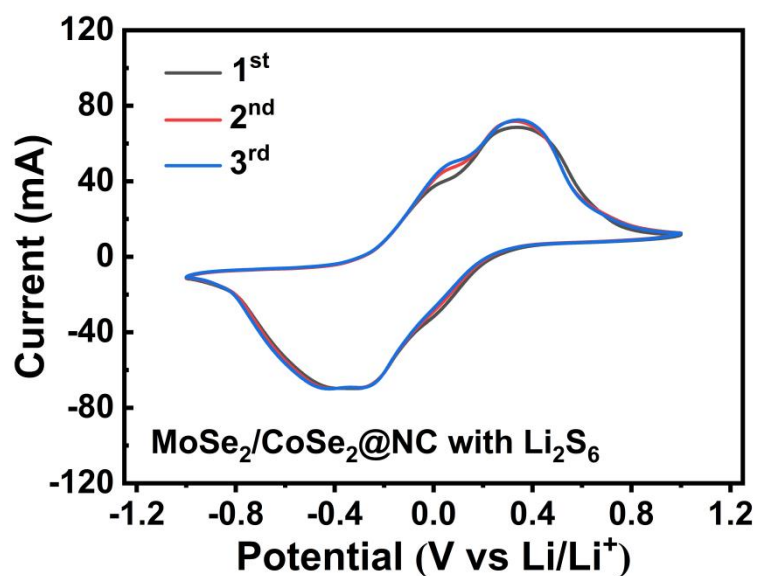
the intrinsic resistance of current collectors, active materials, electrolyte and separator;

R_s: The internal resistance of the solid electrolyte interface (SEI) film correlated with

insoluble Li_2S_2/Li_2S, related to the electrode's surface resistance between the

electrolyte and sulfur electrodes;

R_{ct}: The charge-transfer resistance of sulfur electrode, related to the electrode reaction
kinetics;

CPE1: Capacitance of the electrode bulk in high-frequency region;

CPE2: Capacitance of the charge transfer process at the interface between sulfur and

electrolyte;

W_o: The inclined line in the low frequency is attributed to Warburg impedance (W_0).

The semi-infinite Warburg diffusion impedance of long-chain LiPSs.
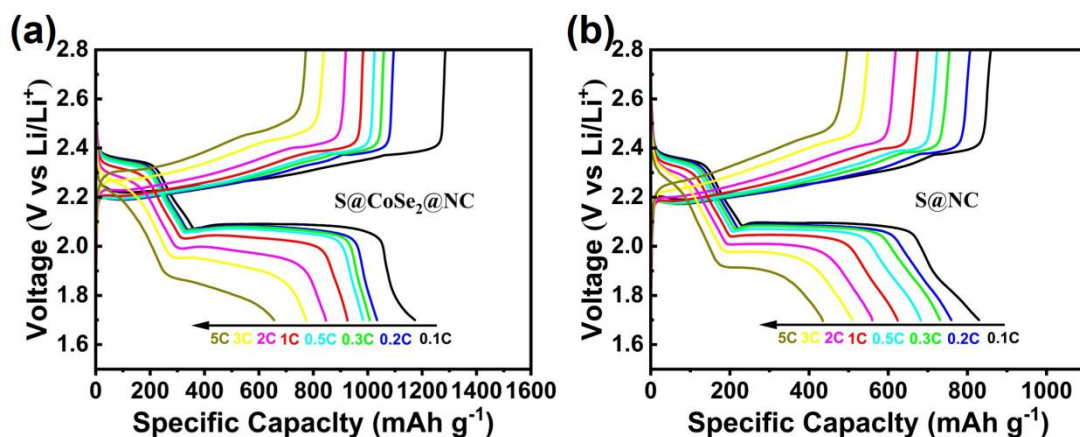
Fig. S24. (a) The charge-discharge curves of S@CoSe$_2$@NC from 0.1 to 5 C; (b) The charge-discharge curves of S@NC from 0.1 to 5 C.

The corresponding galvanostatic discharge/charge plots of S@CoSe$_2$@NC and S@NC cathode materials at a series of current densities. The S@CoSe$_2$@NC cathode delivers initial discharge specific capacity of 1173.47, 1034.14, 1007.20, 982.43, 925.61, 846.62, 774.04 and 655.77 mAh g^{-1} at different rates of 0.1, 0.2, 0.3, 0.5, 1, 2, 3 and 5 C, respectively. However, the S@NC cathode delivers initial discharge specific capacity of 846.04, 759.24, 730.74, 682.31, 623.92, 559.77, 509.21 and 435.00 mAh g^{-1} at different rates of 0.1, 0.2, 0.3, 0.5, 1, 2, 3 and 5 C, respectively.
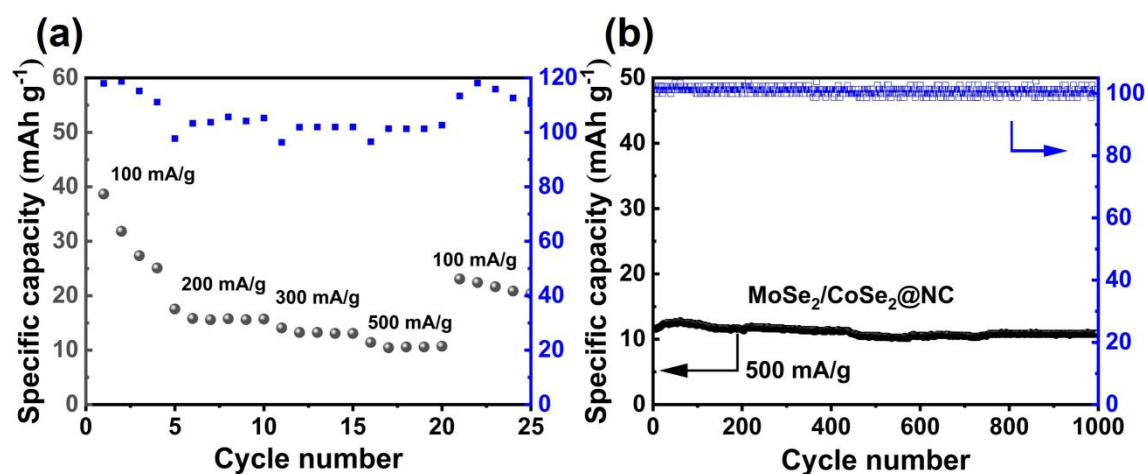
Fig. S25. (a) Rate performance of MoSe$_2$/CoSe$_2$@NC composites at different C-rate,

ranging from 100 to 500 mA g^{-1}; (b) Cycling performance and Coulombic efficiency of MoSe$_2$/CoSe$_2$@NC cathodes at a current rate of 500 mA g^{-1}.

The MoSe$_2$/CoSe$_2$@NC cathode only delivers 38.66, 15.81, 14.08, and 11.41 mAh g^{-1} at current densities of 100, 200, 300, and 500 mA g^{-1}, respectively, which can be ignored.

Fig. S26. (a) SEM and (b) TEM images of S@MoSe$_2$/CoSe$_2$@NC cathode after 100 cycles at 1 C.

Supporting Tables

Table S1. Comparison of equivalent circuit parameters for S@NC, S@CoSe$_2$@NC and S@MoSe$_2$/CoSe$_2$@NC electrodes.

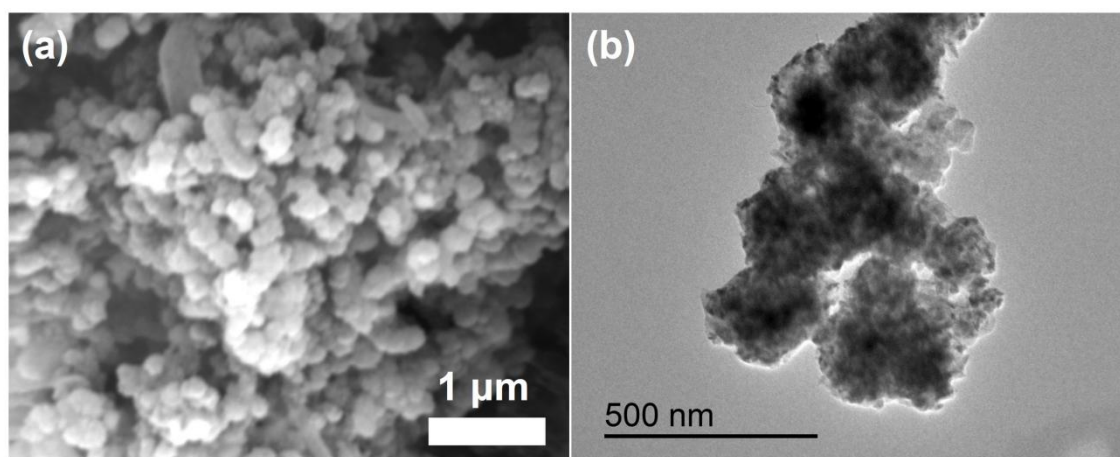| Sample	χ^2	R_0 (Ω)	R_s (Ω)	R_{ct} (Ω)
S@NC	1.52×10^{-3}	6.67	0.95	121.8
S@CoSe$_2$@NC	2.68×10^{-3}	1.77	0.87	65.24
S@MoSe$_2$/CoSe$_2$@NC	2.72×10^{-3}	1.40	0.74	36.61

Table S2. The initial discharge specific capacity (mAh g^{-1}) of S@NC, S@CoSe$_2$@NC and S@MoSe$_2$/CoSe$_2$@NC electrodes at different rates is compared in the rate performance.

	S@NC	S@CoSe$_2$@NC	S@MoSe$_2$/CoSe$_2$@NC
0.1 C	846.04	1173.47	1352.54
0.2 C	759.24	1034.14	1260.62
0.3 C	730.74	1007.20	1197.92
0.5 C	682.31	982.43	1138.49
1 C	623.92	925.61	1051.06
2 C	559.77	846.62	952.79
3 C	509.21	774.04	867.56
5 C	435.00	655.77	729.97
0.1 C	653.71	848.16	986.97

Table S3. Comparison of the electrochemical performance of Li-S batteries with different catalyst.

Host materials	Sulfur content (wt%)	Areal S loading (mg cm^{-2})	Discharge current rate	DIS. capacity (mAh g^{-1}) Initial	DIS. capacity (mAh g^{-1}) After (n^{th})	Ref.
S@MoSe$_2$/CoSe$_2$@NC	**70**	**3.6**	**1 C**	**594**	**472 (100)**	**This work**
		1.5	**3 C**	**820**	**515 (500)**	
		1.5	**1 C**	**993**	**768 (300)**	
S@CoSe$_2$-PNC	60	1.5	1 C	790	546 (300)	[1]
S-Co$_3$O$_4$@MCR	70	1.32	2 C	600	324 (300)	[2]
S@Co/Co$_3$O$_4$-NHC	70	1.2	1 C	617	553 (500)	[3]
NMCS@MoS$_2$/S	70	1.2	0.5 C	894	826 (200)	[4]
MoS$_2$-rGO/S	80	0.85	1 C	872	480 (300)	[5]
Ni$_{0.1}$Zn$_{0.1}$Co$_{0.8}$Se$_2$-S	60	1.0	1 C	679	503 (400)	[6]
S/ZnSe-CoSe$_2$@NC	80	1.23	1 C	810	619 (400)	[7]
CoSe@HPP/S	70	1.2	1 C	912	716 (300)	[8]
MoSe$_2$/N-rGO/S	60	1.1	0.2 C	981	692 (100)	[9]
MoSe$_2$@C/rGO/S	70	1.2	1 C	851	583 (300)	[10]

References

1. F. L. Zhang, H. Wang, S. Ji, V. Linkov, X. Y. Wang and R. F. Wang, *Chemphyschem*, 2022, **23**, 202100811.
2. S. F. Wang, X. H. Hou, Z. M. Zhong, K. X. Shen, G. Z. Zhang, L. M. Yao and F. M. Chen, *Scientific Reports*, 2018, **8**, 16133.
3. Y. Jeon, J. Lee, H. Jo, H. Hong, L. Y. S. Lee and Y. Z. Piao, *Chemical Engineering Journal*, 2021, **407**, 126967.
4. S. X. Jiang, M. F. Chen, X. Y. Wang, Z. Y. Wu, P. Zeng, C. Huang and Y. Wang, *Acs Sustainable Chemistry & Engineering*, 2018, **6**, 16828.
5. Y. You, Y. W. Ye, M. L. Wei, W. J. Sun, Q. Tang, J. Zhang, X. Chen, H. Q. Li and J. Xu, *Chemical Engineering Journal*, 2019, **355**, 671.
6. L. P. Chen, Y. H. Xu, G. Q. Cao, H. M. K. Sari, R. X. Duan, J. J. Wang, C. Xie, W. B. Li and X. F. Li, *Advanced Functional Materials*, 2022, **32**, 2107838.
7. J. Xu, L. L. Xu, Z. L. Zhang, B. Sun, Y. Jin, Q. Z. Jin, H. Liu and G. X. Wang, *Energy Storage Materials*, 2022, **47**, 223.
8. Z. Q. Ye, Y. Jiang, L. Li, F. Wu and R. J. Chen, *Advanced Materials*, 2020, **32**, 2002168.
9. H. L. Wong, X. W. Ou, M. H. Zhuang, Z. J. Liu, M. D. Hossain, Y. T. Cai, H. W. Liu, H. B. Lee, C. Z. Wang and Z. T. Luo, *Acs Applied Materials & Interfaces*, 2019, **11**, 19986.
10. C. C. Li, W. N. Ge, S. Y. Qi, L. Zhu, R. Z. Huang, M. W. Zhao, Y. T. Qian and L. Q. Xu, *Advanced Energy Materials*, 2022, **12**, 2103915.